



 Cite this: *RSC Adv.*, 2020, 10, 14033

 Received 29th February 2020
 Accepted 22nd March 2020

DOI: 10.1039/d0ra01928c

rsc.li/rsc-advances

Observation of spin-glass like behavior in the layered oxyselenides $\text{La}_2\text{O}_3(\text{Mn}_{1-x}\text{Co}_x)_2\text{Se}_2$

 Chenhao Gao,^a Shugang Tan,^a *^a Cao Wang,^a Yuping Sun,^a Rui Cao,^b Kezhen Han,^a Qiang Jing,^a Tong Zhou,^a Qingkuan Meng^a and Fei Xing^a

We have synthesized a new series of layered oxyselenides $\text{La}_2\text{O}_3(\text{Mn}_{1-x}\text{Co}_x)_2\text{Se}_2$ through a solid state reaction method. Their structure and physical properties were studied through powder X-ray diffraction, electric transport measurements, absorption spectroscopy, bulk magnetization and specific heat experiments. These compounds crystallize in layered structures with the space group $I4/mmm$. All the samples present semiconducting or insulating behavior with the activation energy ranging from 0.134 eV to 0.400 eV. The ferromagnetic (FM) component is induced as Co enters the lattice, and the FM component raises to its maximum when x is 0.6. The competing of FM and antiferromagnetic (AFM) components led to the emergence of a spin-glass like behavior in the intermediate alloys.

Introduction

Transition-metal compounds with layered structures have been the focus of experimental and theoretical research for decades due to their unusual physical properties, such as superconductivity in cuprates, and charge density wave (CDW) in transition metal dichalcogenides (TMDC) *etc.*¹

As the requirements of the chemical environment for different anions are different, compounds with mixed anions tend to form layered structures.² For instance, the parent compound of the FeAs-based superconductor LaOFeAs is built with oxide layer $[\text{La}_2\text{O}_2]$ and arsenide layer $[\text{Fe}_2\text{As}_2]$. The superconductivity with $T_C = 26$ K was discovered when F was doped in the O site,³ which set off a new upsurge of the study of Fe-based superconductivity in LnOFeAs .^{4–8} Recently, a new layered compound ThFeAsN , which is crystallized with arsenide layer $[\text{Fe}_2\text{As}_2]$ and nitride layer $[\text{Th}_2\text{N}_2]$, was synthesized and show superconductivity below 30 K.^{9,10} Additionally, another family of the 1111-type layered compound ACuS ($A = \text{LaO}, \text{SrF}, \text{and BaF}$) crystallizes with sulfide layer $[\text{Cu}_2\text{S}_2]$ and oxide or fluoride A layer.^{11–14} The analog BiCuSeO have attracted much attention in thermoelectric field.^{15–18} Quasi-two-dimensional metallic CuSe-based layered compound $\text{Bi}_2\text{YO}_4\text{Cu}_2\text{Se}_2$ is crystallized with edge-shared CuSe_4 tetrahedron layers with Bi_2LnO_4 layers alternatively along the c axis.¹⁹

The parent compounds of cuprates and iron-based superconductors are layered transition metal compounds with an AFM ground state. Therefore, transition metal compounds with mixed anions have important application prospects in the search for new superconducting materials. Recently, a new family of layered TM oxychalcogenides $\text{Ln}_2\text{O}_3\text{TM}_2\text{Ch}_2$ ($\text{Ln} = \text{rare earth}, \text{TM} = \text{Mn}, \text{Fe}, \text{Co}, \text{and Ch} = \text{S}, \text{Se}$) has gathered much attention because of their novel magnetic properties and Mott insulating behaviour.^{20–27} It crystallizes with oxide layer $[\text{Ln}_2\text{O}_2]^{2+}$, which is the same as the Ln_2O_2 layer in LaOFeAs , and $[\text{TM}_2\text{OCh}_2]^{2-}$ layer, which contains the anti-structure of CuO_2 plane in cuprate superconductor. Within the $[\text{TM}_2\text{OCh}_2]^{2-}$ layers transition metal atoms are located at the distorted octahedral environment due to the different distances of TM-Ch and TM-O. The $[\text{TM}_2\text{OCh}_2]^{2-}$ layers in the crystal structure harbor three principal competing interactions.^{23,24} The parent $\text{La}_2\text{O}_3\text{-Mn}_2\text{Se}_2$ has a G-type AFM structure with the ordered moment along the c -axis direction.²¹ On the other hand, $\text{La}_2\text{O}_3\text{Fe}_2\text{Se}_2$ and $\text{La}_2\text{O}_3\text{Co}_2\text{Se}_2$ adopt magnetic structure similar to that of $\text{Fe}_{1.086}\text{Te}$, with the majority spin direction in the ab plane.^{23,28,29} The evolution of structure and magnetic properties tuned by Fe/Mn ratio in $\text{La}_2(\text{Fe}_{1-x}\text{Mn}_x)_2\text{Se}_2\text{O}_3$ was subsequently investigated, which show a rich magnetic phase diagram.²⁶ The study on $\text{Sr}_2\text{F}_2\text{Fe}_2\text{OS}_2$ has revealed a two-Q noncollinear AFM structure which may be suitable for realizing topological spin structures in this family of oxychalcogenides.³⁰ Mott insulating behavior in these oxychalcogenides has been indicated through transport measurements and density functional theory calculations, which is a result of the narrow transition metal 3d band.

In this work, we successfully synthesized a new series of $\text{La}_2\text{O}_3(\text{Mn}_{1-x}\text{Co}_x)_2\text{Se}_2$ compounds and studied evolution of their structural and physical properties.

^aSchool of Physics and Optoelectronic Engineering, Shandong University of Technology, Zibo 255000, People's Republic of China. E-mail: tanshugang@sdut.edu.cn

^bOffice of International Cooperation and Exchange, Shandong University of Technology, Zibo 255000, People's Republic of China



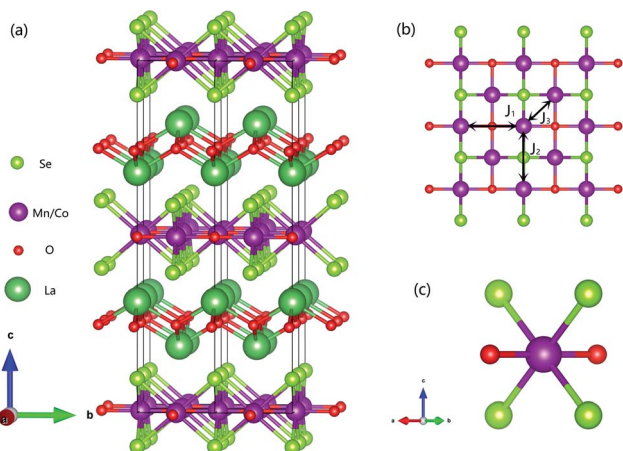


Fig. 1 (a) Crystal structure of $\text{La}_2\text{O}_3(\text{Mn}_{1-x}\text{Co}_x)_2\text{Se}_2$. (b) $(\text{Mn}_{1-x}\text{Co}_x)_2\text{OSe}_2$ planes shown from a vertical view and three principle interactions. (c) The distorted octahedral environment of (Mn, Co) ion.

Experimental details

$\text{La}_2\text{O}_3(\text{Mn}_{1-x}\text{Co}_x)_2\text{Se}_2$ ($0 \leq x \leq 1$) samples were synthesized through solid state reaction method. The samples were prepared by reacting high-purity La_2O_3 (99.9%), Mn (99.9%), Co (99.9%), and Se (99.95%) in a ratio 1 : 2–2x : 2x : 2. La_2O_3 was dried at 1000 °C for 10 hours before use. The raw materials were thoroughly mixed and ground in an agate pestle and mortar, and then the mixtures were pressed into pellets under 12 MPa. The pellets were placed into dried alumina crucibles and sealed under vacuum ($<10^{-4}$ Pa) in the silica tubes which had been baked in dry box for 1–2 hours at 150 °C. The ampoules were annealed at 400 °C for 10 h to ensure the complete reaction of selenium with the elemental metals. The ampoules were then heated to 1000 °C at 1 °C min^{-1} and kept at this temperature for 30 hours. Finally, the furnace was shut down and cool to room temperature naturally. The obtained samples were reground, pelletized, and heated for another 30 hours at 1000 °C followed by furnace cooling. X-ray diffraction (XRD) was performed with an 18 kW X-ray diffractometer with high-intensity Cu $K\alpha$

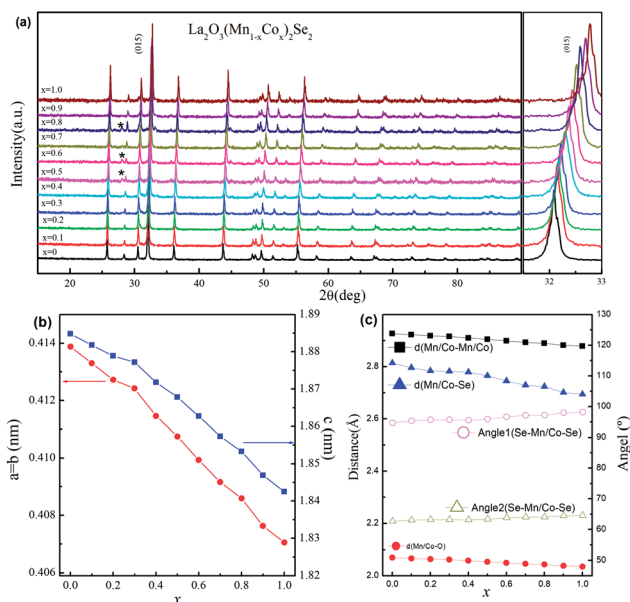


Fig. 2 (a) The powder X-ray diffraction patterns of $\text{La}_2\text{O}_3\text{Mn}_2\text{Se}_2$ at room temperature. The stars represent unknown impurity. The right inset is the enlarged view of the (015) peak ranging from 32° to 33°; (b) the fitted lattice parameters; (c) the evolution of the distances of the nearest Mn/Co–Mn/Co, Mn/Co–O, Mn/Co–Se, and the bond angles of Se–Mn/Co–Se.

radiation. Rietveld refinement of structural parameters was carried out by using RIETICA software.³¹ Thermal, transport, magnetic measurements and heat capacity were carried out in a Quantum Design PPMS-9 and MPMS-5.

Results and discussion

Crystal structures and compositions

Fig. 1(a) shows the crystal structure of $\text{La}_2\text{O}_3(\text{Mn}_{1-x}\text{Co}_x)_2\text{Se}_2$, which is built up by stacking $[\text{La}_2\text{O}_2]$ and $[(\text{Mn}_{1-x}\text{Co}_x)_2\text{Se}_2\text{O}]$ layers alternatively along c axis. The transition-metal (Mn/Co) ions are in square-planar environments in this compound.

Table 1 The room temperature structure details of $\text{La}_2\text{O}_3(\text{Mn}_{1-x}\text{Co}_x)_2\text{Se}_2$ through XRD Rietveld refinement

x	a (Å)	c (Å)	V (Å ³)	$d_{\text{Mn/Co-Mn-Co}}$ (Å)	$d_{\text{Mn/Co-O}}$ (Å)	$d_{\text{Mn-Co-Se}}$ (Å)	R_p (%)	R_{wp} (%)	χ^2
0.0	4.1388(2)	18.848(1)	322.87(2)	2.9266(1)	2.0694(1)	2.814(3)	3.285	5.489	4.257
0.1	4.1330(2)	18.818(1)	321.44(2)	2.9225(1)	2.0665(1)	2.796(2)	4.367	6.495	2.458
0.2	4.1272(2)	18.789(1)	320.05(2)	2.9187(1)	2.0636(1)	2.784(3)	5.994	7.588	1.787
0.3	4.1242(1)	18.772(1)	319.29(2)	2.9162(1)	2.0621(1)	2.782(3)	5.210	7.235	1.625
0.4	4.1146(2)	18.718(1)	316.93(3)	2.9096(1)	2.0574(1)	2.779(2)	5.254	7.528	2.312
0.5	4.1075(2)	18.678(1)	315.12(3)	2.9045(1)	2.0538(1)	2.765(4)	6.035	7.149	2.425
0.6	4.0993(2)	18.627(1)	313.02(2)	2.8987(1)	2.0497(1)	2.745(3)	5.556	7.230	1.625
0.7	4.0916(1)	18.573(1)	310.94(2)	2.8932(1)	2.0458(1)	2.729(2)	5.750	7.274	1.523
0.8	4.0859(2)	18.533(1)	309.36(2)	2.8892(1)	2.0430(1)	2.724(3)	5.253	6.124	1.650
0.9	4.0763(1)	18.469(1)	306.88(2)	2.8823(1)	2.0381(1)	2.701(2)	5.124	7.254	1.772
1.0	4.0705(1)	18.425(1)	305.24(3)	2.8783(1)	2.0353(1)	2.694(3)	6.427	8.351	2.145

Fig. 1(b) shows the $(\text{Mn}_{1-x}\text{Co}_x)_2\text{OSe}_2$ plane from a vertical view with Se atoms puckering above and below the square $(\text{Mn}_{1-x}\text{Co}_x)_2\text{O}$ flat. As shown, there are three main magnetic interactions J_1 – J_3 between Mn/Co ions: the superexchange

interaction of Mn/Co–O–Mn/Co (J_1), the superexchange interaction of Mn/Co–Se–Mn/Co (J_2), the interaction of nearest Mn/Co atoms in the ab plane (J_3). Fig. 1(c) shows the distorted octahedral environment of Mn/Co ions.

We performed the X-ray diffraction experiments on the synthesized samples. Fig. 2(a) shows the powder XRD patterns of $\text{La}_2\text{O}_3(\text{Mn}_{1-x}\text{Co}_x)_2\text{Se}_2$ at room temperature. The Bragg diffractions for the polycrystalline $\text{La}_2\text{O}_3(\text{Mn}_{1-x}\text{Co}_x)_2\text{Se}_2$ samples can be well indexed using the tetragonal structure with the space group $I4/mmm$, except for a little unknown impurity (x : 0.5–0.8). The right part of Fig. 2(a) shows the trend of the (015) diffraction peak. The peak gradually shifts to larger angle degree with increasing x , indicating a shrink of the lattice according to the Bragg formula. All the obtained XRD data were fitted using RIETICA software.³¹ The fitted lattice parameter of $\text{La}_2\text{O}_3\text{Mn}_2\text{Se}_2$ and $\text{La}_2\text{O}_3\text{Co}_2\text{Se}_2$ are $a = b = 4.1388(2)$ Å, $c = 18.848(1)$ Å and $a = b = 4.0705(1)$ Å, $c = 18.425(1)$ Å respectively, in agreement with the previous reported values.^{21,25} The evolution of the lattice parameters, the nearest interlayer Mn/Co–Mn/Co distance, together with the Mn/Co–O and Mn/Co–Se bond distances are shown in Fig. 2(b) and (c) and Table 1. Furthermore, we calculated the valence of Mn and Co ions using the bond valence sum (BVS) formalism in which each bond with a distance d_{ij} contributes a valence $V_{ij} = \exp\left[\frac{(R_{ij} - d_{ij})}{0.37}\right]$ with R_{ij} as an empirical parameter and the total of valences of atom i , V_i equals $V_i = \sum_j V_{ij}$. The calculated valence of Mn and Co ions is +1.99 and +1.96, consistent with the apparent oxidation state (+2) for Mn and Co ions. It should be noted that the lattice parameters decreased linearly with increasing x , which indicates the size of Co^{2+} is smaller than Mn^{2+} . It has been indicated that Co^{2+} is in high spin state. The radius of Co^{2+} in high spin state is 0.0745 nm, while the radius of Mn^{2+} is 0.067 nm in low spin state and 0.083 nm in high spin state. As a result, the Mn^{2+} should be in high spin state.

Electrical transport properties

The main paragraph text follows directly on here. The temperature-dependent resistivity of $\text{La}_2\text{O}_3(\text{Mn}_{1-x}\text{Co}_x)_2\text{Se}_2$ is shown in Fig. 3(a), which exhibit semiconducting or insulating behavior. The $\rho(T)$ of $\text{La}_2\text{O}_3\text{Co}_2\text{Se}_2$ is larger than that of $\text{La}_2\text{O}_3\text{Mn}_2\text{Se}_2$ at all the measured temperature range, which is consistent with previous results. All the resistivity curves can be fitted through the thermal activated model:

$$\rho(T) = \rho_0 e^{\frac{E_g}{k_B T}},$$

where ρ_0 is the prefactor, E_a is the activation energy, k_B is the Boltzmann's constant, and T is thermodynamic temperature. Fig. 3(b) shows the fitting results of the series of samples. The obtained activation energy of $\text{La}_2\text{O}_3\text{Mn}_2\text{Se}_2$ is 0.134 eV and this is considerable smaller than the activation energy of $\text{La}_2\text{O}_3\text{Co}_2\text{Se}_2$ (0.400 eV), which is consistent with the previous results. Neglecting grain boundaries, the

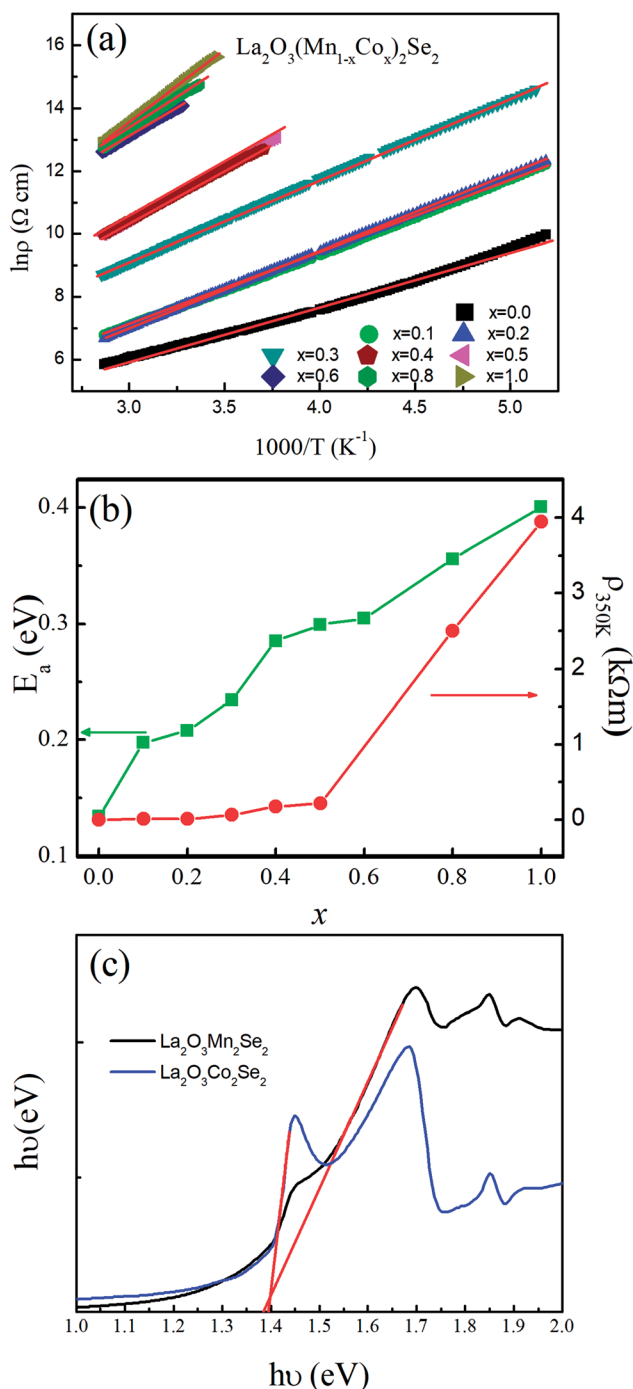


Fig. 3 (a) The temperature dependence of the resistivity for La_2O_3 – $(\text{Mn}_{1-x}\text{Co}_x)_2\text{Se}_2$. The red lines show the fitting result through the thermal activated model. (b) The fitted activation energies and the resistivity at 350 K. (c) The electronic absorption of $\text{La}_2\text{O}_3\text{Mn}_2\text{Se}_2$ and $\text{La}_2\text{O}_3\text{Co}_2\text{Se}_2$. It is the plot of $(\alpha h\nu)^2$ versus photon energy $h\nu$ and the band-gap energy is deduced from the extrapolation of the red straight line up to $(\alpha h\nu)^2 = 0$.

resistivity of polycrystalline $\text{La}_2\text{O}_3\text{Mn}_2\text{Se}_2$ is smaller than $\text{La}_2\text{O}_3\text{Co}_2\text{Se}_2$. Previous studies of $\text{A}_2\text{F}_2\text{Fe}_2\text{OQ}_2$ ($\text{A} = \text{Sr}, \text{Ba}; \text{Q} = \text{S}, \text{Se}$) have indicated that they are Mott insulators with narrowing 3d electronic bands due to strong correlation effects.³² The distance of the nearest Mn/Co–Mn/Co becomes smaller with increasing x . In the viewpoint of electron hopping between adjacent unpaired spins in Mn/Co site, it is more difficult for electron hopping with larger distance, which is inconsistent with our results. The result suggests that the 3d electrons of Co are practically localized. We took the measurements of the absorption spectra of $\text{La}_2\text{O}_3\text{Mn}_2\text{Se}_2$ and $\text{La}_2\text{O}_3\text{Co}_2\text{Se}_2$, as shown in Fig. 3(c). The optical energy band gap can be determined from the sharp decrease in the transmission region according to Tauc and Menth's law. It can be seen that the band gap of $\text{La}_2\text{O}_3\text{Co}_2\text{Se}_2$ (1.40 eV) is slightly larger than $\text{La}_2\text{O}_3\text{Mn}_2\text{Se}_2$ (1.38 eV). The difference of the electric band structure needs to be further studied by DFT calculations. It can be speculated that $\text{La}_2\text{O}_3\text{Co}_2\text{Se}_2$ may have a larger effective mass of electron if the transport behaviors are intrinsic.

Magnetic properties

The temperature dependence of dc magnetic susceptibility taken in magnetic field $H = 1000$ Oe for $\text{La}_2\text{O}_3(\text{Mn}_{1-x}\text{Co}_x)_2\text{Se}_2$ with zero field cooling (ZFC) and field cooling (FC) modes are shown in Fig. 4. There is a clear difference between the curves obtained for zero-field-cooling (ZFC) and field-cooling (FC) samples. For undoped $\text{La}_2\text{O}_3\text{Mn}_2\text{Se}_2$,

there are several features in the curve. There is a broad maximum near 250 K, and no Curie–Weiss behavior up to 350 K, indicating the existence of 2D short-range ordering

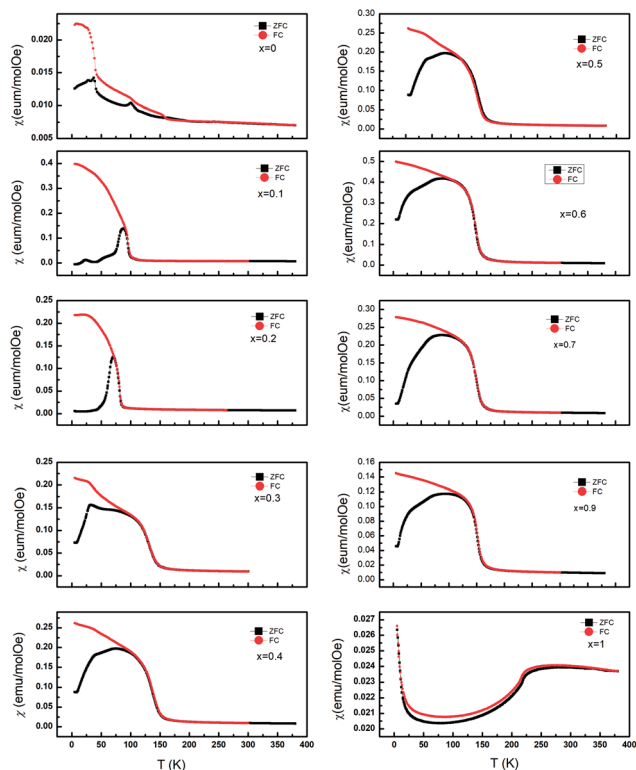


Fig. 4 The temperature dependence of the magnetic susceptibility $\chi(T)$ for $\text{La}_2\text{O}_3(\text{Mn}_{1-x}\text{Co}_x)_2\text{Se}_2$ taken in 1000 Oe.

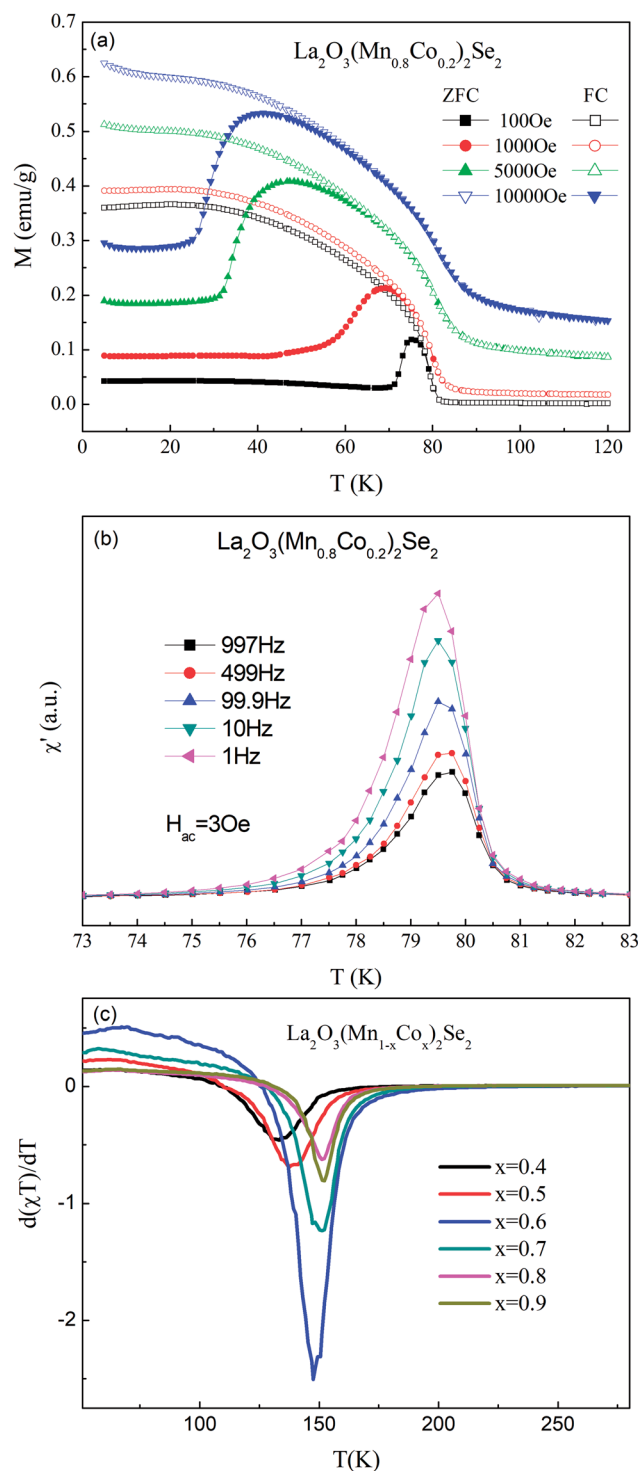


Fig. 5 (a) Zero-field-cooled and field-cooled magnetic susceptibilities for $\text{La}_2\text{O}_3(\text{Mn}_{0.8}\text{Co}_{0.2})_2\text{Se}_2$ measured under various magnetic fields. (b) Temperature dependence of $\chi'(T)$ measured at different fixed frequencies for $\text{La}_2\text{O}_3(\text{Mn}_{0.8}\text{Co}_{0.2})_2\text{Se}_2$. (c) $d(\chi T)/dT$ of $\text{La}_2\text{O}_3(\text{Mn}_{1-x}\text{Co}_x)_2\text{Se}_2$ ($0.4 \leq x \leq 0.9$).

in this compound at high temperature. At low temperature, the ZFC curve exhibits two anomalies at about 37 K (T_1) and 101 K (T_2), and the susceptibility increase with decreasing temperature, which suggests the presence of ferromagnetic component due to the occurrence of spin reorientation in this anisotropic magnetic system. Similar behaviors have been reported in previous literatures.^{25,26} With Co doping, the broad maximum disappears. The cusp at T_1 rapidly shifts to lower temperature and disappears for $x = 0.2$. The cusp at T_2 gradually shifts to lower temperature and a spin-glass like behavior emerges ($x = 0.1, 0.2$). We performed the magnetic susceptibility for $\text{La}_2\text{O}_3(\text{Mn}_{0.8}\text{Co}_{0.2})_2\text{Se}_2$ under various fields in Fig. 5(a). The freezing temperature shifts to lower temperature with higher fields, suggesting the glass like state at low temperature. As known, frequency dependences of ac susceptibility $\chi'(T)$ is needed to confirm the characteristics of the spin-glass (SG) like behavior. We performed the measurement of the frequency dependences of ac susceptibility $\chi'(T)$ for $\text{La}_2\text{O}_3(\text{Mn}_{0.8}\text{Co}_{0.2})_2\text{Se}_2$. Fig. 5(b) displays the $\chi'(T)$ for $\text{La}_2\text{O}_3(\text{Mn}_{0.8}\text{Co}_{0.2})_2\text{Se}_2$ as a function of temperature under an ac field of $H_{\text{ac}} = 3$ Oe with several fixed frequencies ($1 \leq f \leq 1000$ Hz). We find the peak in the real part of ac susceptibility $\chi'(T)$ exhibits frequency dependence with the ac magnetic field. We determined the positions of the peaks through polynomial fitting near the peaks, as the change in the position of the peak is very small. The peak position shifts to higher temperatures and the magnitude decreases with increasing frequency, which is a typical SG behavior. We fitted the frequency dependence of the peak shift using $K = \Delta T_f / (T_f \Delta \log f)$ and obtained $K = 0.0013$, which is slightly smaller than the values found in canonical SG system.³³

For $x > 0.4$, FM-like behavior emerges. We performed the $d(\chi T)/dT$ curves ranging from 100 K to 200 K in Fig. 5(c). For $0.4 \leq x \leq 0.9$, the temperature of the minimum of the $d(\chi T)/dT$ curves shifts to lower temperature with increasing Co content, and the value of the minimum increase initially and decrease afterwards. Fig. 6 displays the isothermal $M(H)$ curves. For $\text{La}_2\text{O}_3\text{Mn}_2\text{Se}_2$ and $\text{La}_2\text{O}_3\text{Co}_2\text{Se}_2$, the $M(H)$ curves are almost linear, indicating the AFM interaction is dominant at low

temperature. For the intermediate alloy samples, non-zero remanent magnetization and finite coercive field emerge in the hysteresis measurements, indicating the existence of FM component. The $M(H)$ curves also reveal the FM component increase initially and decrease afterwards, which is consistent with the result obtained above. Overall, with Co doing in $\text{La}_2\text{O}_3\text{Mn}_2\text{Se}_2$, the FM component of magnetization increase, which may be induced by frustration, canting, or anisotropic exchange interactions.²⁶ The competition between AFM and FM interaction in the $(\text{Mn}_{1-x}\text{Co}_x)_2\text{OSe}_2$ layer leads to the emergence of spin-glass like state. When Co is dominating, the FM component decrease and a new long-range order is built. Similar behaviors have been reported in $\text{Sr}_2\text{Co}_{1-x}\text{Mn}_x\text{O}_2\text{Cu}_2\text{Se}_2$, in which Mn/Co ions are also located at quasi 2D planes.³⁴

Heat capacity

Fig. 7 shows the specific heat of the samples. The specific heat of all the samples approach the value of $3NR$ at 300 K, where N is the number of atoms in the chemical formula ($N = 9$) and R is the gas constant ($R = 8.31 \text{ J mol}^{-1} \text{ K}^{-1}$), consistent with the Dulong–Petit law. There is no anomaly for $\text{La}_2\text{O}_3\text{Mn}_2\text{Se}_2$ at the temperature where the magnetic susceptibility has anomalies. On the other hand, the specific heat of $\text{La}_2\text{O}_3\text{Co}_2\text{Se}_2$ shows a λ -type anomaly at about 218 K (T_λ), which is due to the long-range three-dimensional AFM ordering of Co^{2+} . The magnetic contribution to the heat capacity can be obtained by subtracting the phonon contribution fitted using a polynomial from the total specific heat. The magnetic entropy is calculated using $S_{\text{mag}}(T) = \int_0^T \frac{C_{\text{mag}}}{T} dT$. The derived S_{mag} is $5.6 \text{ J mol}^{-1} \text{ K}^{-1}$ at 250 K, which is much smaller than the expected value for Co^{2+} ions with high spin state [$\sim 48\% R \ln(2S + 1) = R \ln 5$]. For $x = 0.9$ the T_λ shifts to lower temperature. For $\text{La}_2\text{O}_3\text{MnCoSe}_2$, no anomaly was detected. This phenomenon is consistent with previous results. It can be explained as follows. As shown in figure, for $\text{La}_2\text{O}_3\text{Co}_2\text{Se}_2$, there is a broad maximum in the $\chi(T)$ curve and no Curie–Weiss behavior was detected up to 350 K, which may be due to a possible 2D short-range magnetic order before 3D long range magnetic order correlation develop. And a substantial fraction of magnetic entropy is locked due to the 2D short-

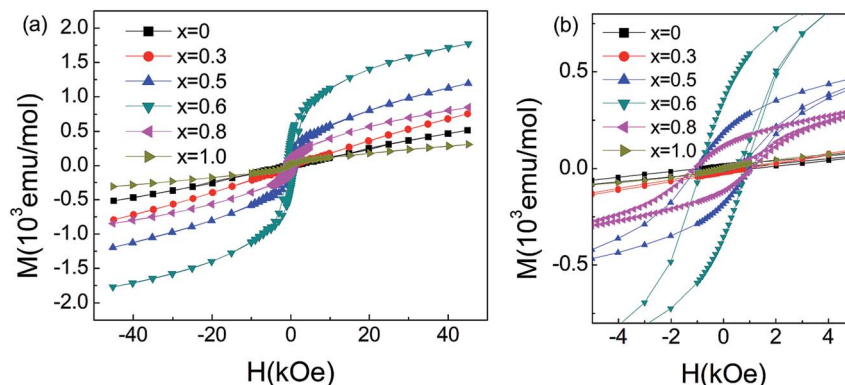


Fig. 6 (a) Magnetic moment for $\text{La}_2\text{O}_3(\text{Mn}_{1-x}\text{Co}_x)_2\text{Se}_2$ as a function of field measured at 5 K. (b) The magnified plot of $M-H$ at low fields.

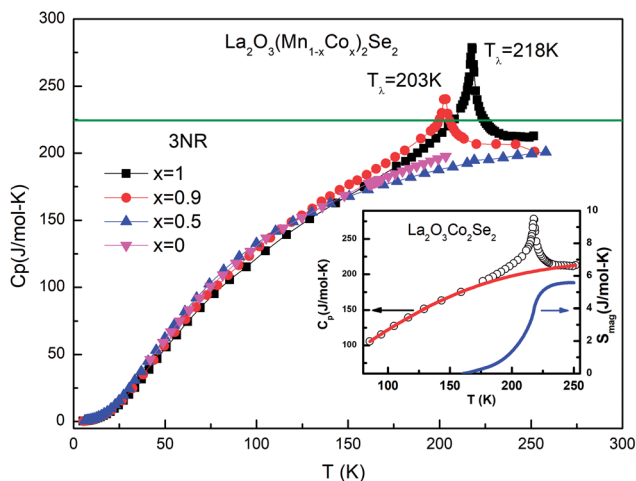


Fig. 7 The temperature dependence of the specific heat for $\text{La}_2\text{O}_3(\text{Mn}_{1-x}\text{Co}_x)_2\text{Se}_2$ ($x = 0, 0.5, 0.9, 1$). Inset shows the specific heat of $\text{La}_2\text{O}_3\text{Co}_2\text{Se}_2$ data between 80 K and 250 K. The red curve represents the phonon contribution to the total specific heat. The blue curve denotes the magnetic entropy $S_{\text{mag}}T = \int_0^T \frac{C_{\text{mag}}}{T} dT$.

range magnetic order. With the increase of Mn content, the λ -anomaly disappear, resulting from the overwhelming release of magnetic entropy due to the existence of 2D short-range order.

Conclusions

In summary, we synthesized a series of layered oxyselenide $\text{La}_2\text{O}_3(\text{Mn}_{1-x}\text{Co}_x)_2\text{Se}_2$ through solid state reaction method. The structural and physical properties were thoroughly investigated. All the samples present semiconducting or insulating behavior with the activation energy ranging from 0.134 eV to 0.400 eV. FM component is induced as Co enters the lattice, and the FM component raise to a maximum as x is 0.6. The competing of AFM and FM induced a spin-glass like behavior in the intermediate alloy compounds.

Conflicts of interest

There are no conflicts to declare.

Acknowledgements

This work was supported by the National Nature Science Foundation of China under contract No. 51802177 and No. 11804194, the Natural Science Foundation of Shandong Province under grand No. ZR2019MA020, and the Research Start-up Funds of Shandong University of Technology (No. 415058).

Notes and references

1 R. Cava, *Science*, 1990, **247**, 656.

- S. J. Clarke, P. Adamson, S. J. C. Herkelrath, O. J. Rutt, D. R. Parker, M. J. Pitcher and C. F. Smura, *Inorg. Chem.*, 2008, **47**, 8473.
- Y. Kamihara, T. Watanabe, M. Hirano and H. Hosono, *J. Am. Chem. Soc.*, 2008, **130**, 3296.
- X. H. Chen, T. Wu, G. Wu, R. H. Liu, H. Chen and D. F. Fang, *Nature*, 2008, **453**, 761.
- Z. A. Ren, J. Yang, W. Lu, W. Yi, G. C. Che, X. L. Dong, L. L. Sun and Z. X. Zhao, *Mater. Res. Innovations*, 2008, **12**, 105.
- Z. A. Ren, J. Yang, W. Lu, W. Yi, X. L. Shen, Z. C. Li, G. C. Che, X. L. Dong, L. L. Sun, F. Zhou and Z. X. Zhao, *Europhys. Lett.*, 2008, **82**, 57002.
- G. F. Chen, Z. Li, D. Wu, G. Li, W. Z. Hu, J. Dong, P. Zheng, J. L. Luo and N. L. Wang, *Phys. Rev. Lett.*, 2008, **100**, 247002.
- C. Wang, Z.-C. Wang, Y.-X. Mei, Y.-K. Li, L. Li, Z.-T. Tang, Y. Liu, P. Zhang, H.-F. Zhai, Z.-A. Xu and G.-H. Cao, *J. Am. Chem. Soc.*, 2016, **138**, 2170.
- H. Wang, J. Guo, Y. Shao, C. Wang, S. Cai, Z. Wang, X. Li, Y. Li, G. Cao and Q. Wu, *Europhys. Lett.*, 2018, **123**, 67004.
- J. Yang, X. L. Shen, W. Lu, W. Yi, Z. C. Li, Z. A. Ren, G. C. Che, X. L. Dong, L. L. Sun, F. Zhou and Z. X. Zhao, *New J. Phys.*, 2008, **11**, 025005.
- M. C. R. Palazzi, *C. R. Seances Acad. Sci., Ser. C*, 1981, **292**, 7899.
- H. Kabbour, L. Cario, S. Jobic and B. Corraze, *J. Mater. Chem.*, 2016, **16**, 4165.
- H. Yanagi, J. Tate, S. Park, C.-H. Park, D. A. Keszler, M. Hirano and H. Hosono, *J. Appl. Phys.*, 2006, **100**, 083705.
- L. D. Zhao, D. Berardan, Y. L. Pei, C. Byl, L. Pinsard-Gaudart and N. Dragoë, *Appl. Phys. Lett.*, 2010, **97**, 092118.
- Y. Liu, L. D. Zhao, Y. Liu, J. Lan, W. Xu, F. Li, B. P. Zhang, D. Berardan, N. Dragoë, Y. -H. Lin, C. W. Nan, J. -F. Li and H. Zhu, *J. Am. Chem. Soc.*, 2011, **133**, 20112.
- G.-K. Ren, S. Wang, Z. Zhou, X. Li, J. Yang, W. Zhang, Y.-H. Lin, J. Yang and C.-W. Nan, *Nat. Commun.*, 2019, **10**, 2814.
- S. Tan, C. Gao, C. Wang, Y. Sun, Q. Jing, Q. Meng, T. Zhou and J. Ren, *Solid State Sci.*, 2019, **98**, 106019.
- A. Zakutayev, J. Tate and G. Schneider, *Phys. Rev. B*, 2010, **82**, 195204.
- S. G. Tan, D. F. Shao, W. J. Lu, B. Yuan, Y. Liu, J. Yang, W. H. Song, H. Lei and Y. P. Sun, *Phys. Rev. B*, 2014, **90**, 085144.
- J. M. Mayer, L. F. Schneemeyer, T. Siegrist, J. V. Waszczak and B. V. Dover, *Angew. Chem., Int. Ed. Engl.*, 1992, **31**, 1645.
- C. Wang, M. Q. Tan, C. M. Feng, Z. F. Ma, S. Jiang, Z. A. Xu, G. H. Cao, K. Matsubayashi and Y. Uwatoko, *J. Am. Chem. Soc.*, 2010, **132**, 7069.
- Y. Fuwa, T. Endo, M. Wakeshim, Y. Hinatsu and K. Ohoyama, *J. Am. Chem. Soc.*, 2010, **132**, 18020.
- D. G. Free, N. D. Withers, P. J. Hickey and J. S. O. Evans, *Chem. Mater.*, 2011, **23**, 1625.
- N. Ni, S. Jia, Q. Huang, E. Climent-Pascual and R. J. Cava, *Phys. Rev. B*, 2011, **83**, 224403.
- Y. Fuwa, M. Wakeshima and Y. Hinatsu, *J. Phys.: Condens. Matter*, 2010, **22**, 346003.

- 26 H. C. Lei, E. S. Bozin, A. Llobet, V. Ivanovski, V. Koteski, J. Belosevic-Cavor, B. Cekic and C. Petrovic, *Phys. Rev. B*, 2012, **86**, 125122.
- 27 S. Landsgesell, E. Blumenröther and K. Prokeš, *J. Phys.: Condens. Matter*, 2013, **25**, 086004.
- 28 D. G. Free and J. S. O. Evans, *Phys. Rev. B*, 2010, **81**, 214433.
- 29 S. Li, C. de la Cruz, Q. Huang, Y. Chen, J. W. Lynn, J. Hu, Y. L. Huang, F. C. Hsu, K. W. Yeh, M. K. Wu and P. C. Dai, *Phys. Rev. B*, 2009, **79**, 054503.
- 30 K. W. Bayliff, S. Wu, V. Loganathan, L. L. Zhao, J. K. Wang, A. H. Nevidomskyy, C. Broholm, C.-L. Huang and E. Morosan, *Phys. Rev. B*, 2019, **99**, 024412.
- 31 B. Hunter, *International Union of Crystallography Commission on Powder Diffraction Newsletter No. 20*, 1998, <http://www.rietica.rog>.
- 32 H. Kabbour, E. Janod, B. Corraze, M. Danot, C. Lee, M. H. Whangbo and L. Cario, *J. Am. Chem. Soc.*, 2008, **130**, 8261.
- 33 J. A. Mydosh, *Spin Glass: An Experimental Introduction*, Talor & Francis, London, 1993.
- 34 S. G. Tan, H. C. Lei, W. J. Lu, P. Tong, L. J. Li, S. Lin, Y. N. Huang, Z. H. Huang, Y. Liu, B. C. Zhao and Y. P. Sun, *J. Alloys Compd.*, 2014, **598**, 171.